JOURNAL OF GEOPHYSICAL RESEARCH, VOL. 94, NO. A6, PAGES 6523–6538, JUNE 1, 1989

Nonlinear Two-Fluid Hydromagnetic Waves in the Solar Wind: Rotational Discontinuity, Soliton, and Finite-Extent Alfvén Wave Train Solutions

L. H. Lyu and J. R. Kan

Geophysical Institute, University of Alaska, Fairbanks

Nonlinear one-dimensional constant-profile hydromagnetic wave solutions are obtained in finite-temperature two-fluid collisionless plasmas under adiabatic equation of state. The nonlinear wave solutions can be classified according to the wavelength. The long-wavelength solutions are circularly polarized incompressible oblique Alfvén wave trains with wavelength greater than hundreds of ion inertial length. The oblique wave train solutions can explain the high degree of alignment between the local average magnetic field and the wave normal direction observed in the solar wind. The short-wavelength solutions include rarefaction fast solitons, compression slow solitons, Alfvén solitons and rotational discontinuities, with wavelength of several tens of ion inertial length, provided that the upstream flow speed is less than the fast-mode speed. The Alfvén solitons and rotational discontinuities are super-Alfvénic compression waves if the upstream Alfvén-mode speed is greater than the sound speed; otherwise, they are sub-Alfvénic rarefaction waves. The density and magnetic field variations of these short-wavelength waves are shown to obey the following two rules: (1) all compression waves are left-hand polarized and all rarefaction waves are right-hand polarized, due to the ion inertial effect, (2) the density variation and the magnetic field magnitude variation are in phase if the flow is supersonic, but out of phase if the flow is subsonic, which is a consequence of conservation of the momentum flux. The two-fluid rotational discontinuity solution obtained in this study is highly circularly polarized, with a variable angular rotation rate. The total angle of rotation is limited to less than or equal to 180°, which is consistent with the rotational discontinuity observed in the solar wind. The upstream flow speed of the two-fluid rotational discontinuity must deviate slightly from the Alfvén-mode speed; the downstream flow speed is equal to the local sound speed. The formation of the two-fluid rotational discontinuity depends critically on the dispersion effect which converts the Alfvén mode to the ion acoustic mode.

1. Introduction

Rotational discontinuities with structures of a few tens of ion gyroradii have been observed at the magnetopause [e.g., *Sonnerup and Ledley*, 1974] and in the solar wind [e.g., *Martin et al.*, 1973; *Burlaga et al.*, 1977; *Lepping and Behannon*, 1986]. The absence of rotational angle greater than 180° in the highly circularly polarized rotational discontinuity has been reported by *Sonnerup and Cahill* [1968] and demonstrated in the simulation results by *Swift and Lee* [1983]. Theoretical understanding of this particular property of the rotational discontinuity is still lacking.

Paper number 89JA00030
0148-0227/89/89JA-00030$05.00

Since neither the standard MHD Rankine-Hugoniot (R-H) jump condition nor a modified MHD R-H jump condition [e.g., *Hudson*, 1971, 1973] can explain the observed rotational limit in the rotational discontinuity, this feature must be a non-MHD effect. The thickness of the rotational discontinuity observed in the solar wind indicates that the ion inertial effect plays an important role. The simplest plasma model which retains the ion inertial effect is the two-fluid plasma equations [e.g., *Petschek*, 1958; *Fishman et al.*, 1960; *Hain et al.*, 1960; *Stringer*, 1963; *Formisano and Kennel*, 1969]. This fact motivates us to seek nonlinear constant-profile wave solutions in finite-temperature two-fluid plasmas. The solutions obtained in this study consist of long-wavelength wave trains and short-wavelength solitons and rotational discontinuities. Specifically, the 180° rotational limit in the rotational discontinuity is shown to be a basic characteristic of the two-fluid rotational discontinuity solution obtained analytically in this paper.

In addition to the rotational discontinuity, we also address the controversial issue of alignment between the wave normal and the local average magnetic field of nonlinear Alfvénic fluctuations observed in the solar wind. These fluctuations consist of large amplitude waves moving away from the Sun around the Alfvén speed relative to the solar wind. The structure of the low-frequency ($10^{-5} \sim 10^{-3}$ Hz) Alfvénic fluctuations observed in the solar wind is often a finite-extent wave train structure [e.g., *Belcher and Davis*, 1971; *Daily*, 1973]. The magnetic field of the observed wave train structure is highly circularly polarized with a well-defined wave normal direction determined by the minimum variance method [*Sonnerup and Cahill*, 1967]. The wave normal direction of the observed Alfvénic fluctuations is found to be highly parallel to the "local average magnetic field" in both high-speed and low-speed streams of the solar wind and at different heliographic distances [e.g., *Belcher and Davis*, 1971; *Daily*, 1973; *Solodyna and Belcher*, 1976; *Denskat and Neubauer*, 1982]. According to the geometrical optics [e.g., *Hollweg*, 1975], the propagation direction of a planar nonlinear Alfvén wave should be refracted by the velocity shear in the solar wind. Therefore, the geometrical optics predicts that the distribution of the angle between the wave normal and the "upstream magnetic field" should vary with the location of observation and cannot be expected to always peak around zero degree. Under the commonly adopted assumptions that the "local average magnetic field" is equal to the "upstream magnetic field" and that the observed wave normal is parallel to the "local average magnetic field," one is led to the questionable conclusion that the wave normal is parallel to the "upstream magnetic field." This dubious conclusion is in conflict with the prediction of the geometrical optics [e.g., *Solodyna and Belcher*, 1976; *Barnes*, 1981, 1983]. In an attempt to circumvent this conflict, the idea of turbulence is proposed to explain the preferential orientation of the wave normal along the average magnetic field direction [*Barnes*, 1981, 1983; *Matthaeus and Goldstein*, 1982]. On the other hand, *Solodyna and Belcher* [1976] argued that the conflict could be due to inapplicability of the minimum variance method. They even suggest that the minimum variance method cannot determine the wave normal direction, but gives the average magnetic field direction.

In this paper we show that the high degree of alignment between the wave normal and the local average magnetic field is a basic characteristics for both parallel and oblique Alfvén wave train solutions. Therefore, the "local average magnetic field" need not be in the same direction as the ambient magnetic field. Hence, the wave normal of the observed nonlinear Alfvénic fluctuations may indeed oblique to the ambient magnetic field.

Finally, the possible relationship between the soliton solutions obtained in this paper and the turbulent Alfvénic fluctuations observed in the solar wind will be discussed in this paper.

2. FORMULATION

In this study, we seek nonlinear constant-profile ($\partial/\partial t = 0$) one-dimensional ($\nabla = \hat{\mathbf{x}} d/dx$) wave solutions in the collisionless finite-temperature two-fluid plasmas. Based on the pseudo potential method, solutions of nonlinear constant-profile waves in two-fluid plasmas have been obtained in both cold plasma [e.g., *Davis et al.*, 1958; *Montgomery*, 1959; *Saffman*, 1961; *Kellogg*, 1964; *Morton*, 1964; *Cavaliere and Engelmann*, 1967] and finite-temperature plasmas [*Hain et al.*, 1960; *Kakutani et al.*, 1967; *Crevier and Tidman*, 1970; *Coroniti*, 1971; *Churilov*, 1980; *Ziegler and Schindler*, 1988]. However, most of the nonlinear wave studies in the finite-temperature two-fluid plasma emphasized applications to shock structures, since the thickness of shock waves is also of the order of the ion gyroradius. The formulation in this study is similar to the previous studies but generalized to include the rotational discontinuity solutions. To make the present paper self-contained with unified notations, a summary of the formulation is necessary.

Under the quasi-neutrality approximation, the number densities of the ions and electrons are taken to be $n_i \cong n_e = n$. The ion and electron pressures are assumed isotropic and each follows the adiabatic process. The basic equations for these waves are the standard time-independent ($\partial/\partial t = 0$) two-fluid plasma equations which can be simplified and written in the Gaussian units as given below.

The continuity equation (of the αth species, i.e., ions and electrons)

$$\nabla \cdot (\rho_\alpha \mathbf{V}_\alpha) = 0 \tag{1}$$

The momentum equation

$$\mathbf{V}_\alpha \cdot \nabla \mathbf{V}_\alpha + (1/\rho_\alpha)\nabla p_\alpha - (e_\alpha/m_\alpha c)(c\mathbf{E} + \mathbf{V}_\alpha \times \mathbf{B}) = 0 \tag{2}$$

The energy equation

$$(3/2)\mathbf{V}_\alpha \cdot \nabla p_\alpha + (5/2) p_\alpha \nabla \cdot \mathbf{V}_\alpha = 0 \tag{3}$$

The Maxwell equations

$$\nabla \cdot \mathbf{B} = 0 \tag{4}$$

$$\nabla \times \mathbf{E} = 0 \tag{5}$$

$$\nabla \times \mathbf{B} = 4\pi n e(\mathbf{V}_i - \mathbf{V}_e)/c \tag{6}$$

where ions are assumed to be protons, c is the speed of light, e_α, m_α, n_α, $\rho_\alpha (\equiv n_\alpha m_\alpha)$, $\mathbf{V}_\alpha$, and p_α are respectively the charge, mass, number density, mass density, flow velocity, and thermal pressure of the αth species. Note that the Poisson equation can be ignored under the quasi-neutrality approximation.

The boundary condition on the upstream side ($x \to -\infty$) is assumed uniform, namely, all derivatives vanish. Wave propagation is oblique to the upstream magnetic field with a wave normal angle θ_o. We choose the coordinates such that the upstream magnetic field is in the xy-plane, i.e.,$\mathbf{B}_o = [B_{xo}, B_{yo}, 0]$, where the subscript o indicates the upstream quantities. For $B_o = (B_{xo}^2 + B_{yo}^2)^{1/2}$, the wave normal angle becomes $\theta_o = \cos^{-1}(B_{xo}/B_o)$. We choose a moving frame such that the upstream flow velocity is in the x-direction, i.e., the normal incidence frame [e.g., *Goodrich and Scudder*, 1984]. Based on the uniform boundary condition the current density must vanish on the upstream side so that $\mathbf{V}_{io} = \mathbf{V}_{eo} = \mathbf{V}_o = \hat{\mathbf{x}}V_o$ is the upstream flow velocity. Without loss of nonlinearity, we write the total magnetic field $\mathbf{B}(x) = \mathbf{B}_o + \mathbf{b}(x)$. From (4), $B_x = B_{xo}$ =constant, so that $\mathbf{b}(x)$ has only the y and z components, i.e., $\mathbf{b} = [0, b_y, b_z]$. Likewise, (5) leads to constant E_y and E_z. It can be shown that the upstream electric field in the normal incidence frame is given by $\mathbf{E}_o = -\hat{\mathbf{z}}V_oB_{yo}/c$, so that $E_y = E_{yo} = 0$, and $E_z = E_{zo} = -V_oB_{yo}/c$. Based on the quasi-neutrality approximation, (1) leads to $V_{xi}(x) \cong V_{xe}(x) = V_x(x)$. The isentropic equation of state for each species can be obtained from (3), i.e.,

$$p_\alpha V_x^\gamma = p_{\alpha o} V_o^\gamma \tag{7}$$

where $p_{\alpha o}$ are the upstream pressures of the αth species (ions or electrons), and $\gamma \equiv 5/3$.

For constant-profile wave solutions, it is convenient to cast (1)$\sim$(6) into conservative forms. Under the uniform boundary condition, the conservation equations are

conservation of mass flux

$$[\rho_i(x) + \rho_e(x)]\, V_x(x) = \rho_o V_o \tag{8}$$

conservation of momentum flux

$$(p_i + p_e) + \rho_o V_o V_x + \frac{(B_{yo} + b_y)^2 + b_z^2}{8\pi} = p_o + \rho_o V_o^2 + \frac{B_{yo}^2}{8\pi} \tag{9}$$

$$(\rho_i V_{yi} + \rho_e V_{ye}) V_x - \frac{B_{xo} b_y}{4\pi} = 0 \tag{10}$$

$$(\rho_i V_{zi} + \rho_e V_{ze}) V_x - \frac{B_{xo} b_z}{4\pi} = 0 \tag{11}$$

and conservation of energy flux

$$\frac{1}{2}\left[\rho_i\left(V_x^2 + V_{yi}^2 + V_{zi}^2\right) + \rho_e\left(V_x^2 + V_{ye}^2 + V_{ze}^2\right)\right] V_x + \frac{5}{2}(p_i + p_e) V_x + \frac{V_o B_{yo}(B_{yo} + b_y)}{4\pi} = \frac{1}{2}\rho_o V_o^3 + \frac{5}{2} p_o V_o + \frac{V_o B_{yo}^2}{4\pi} \tag{12}$$

where $\rho_o \equiv (m_i + m_e) n_o$ and $p_o \equiv p_{io} + p_{eo}$ are the total mass density and pressure on the upstream side, and n_o is the upstream number density of each species. Note that we have neglected the E^2/B_o^2 terms (of order $V_o^2/c^2 \ll 1$) in (9) and (12).

Defining τ by $d\tau = dx/V_x$ and using the notation $\dot{A} \equiv dA/d\tau \equiv V_x(dA/dx)$ to indicate the convective derivative, the momentum equation (2) can be rewritten in the component form as

$$\dot{V}_{x\alpha} = +(e_\alpha/m_\alpha c)\left[cE_x + V_{y\alpha} b_z - V_{z\alpha}(B_{yo} + b_y)\right] - (1/\rho_o V_o)\dot{p}_\alpha = 0 \tag{13}$$

$$\dot{V}_{y\alpha} = +(e_\alpha/m_\alpha c)\left[V_{z\alpha} B_{xo} - V_x b_z\right] \tag{14}$$

$$\dot{V}_{z\alpha} = +(e_\alpha/m_\alpha c)[-V_o B_{yo} + V_x(B_{yo} + b_y) - V_{y\alpha} B_{xo}] \tag{15}$$

where $\dot{V}_x = \dot{V}_{x\alpha}$ for each species. Likewise, multiplying V_x to (6) leads to

$$\begin{aligned} \dot{b}_y &= +(4\pi e/c) n_o V_o (V_{zi} - V_{ze}) \\ \dot{b}_z &= -(4\pi e/c) n_o V_o (V_{yi} - V_{ye}) \end{aligned} \tag{16}$$

Differentiating (16) once with respect to τ leads to

$$\begin{aligned} \ddot{b}_y &= +(4\pi e/c) n_o V_o \left(\dot{V}_{zi} - \dot{V}_{ze}\right) \\ \ddot{b}_z &= -(4\pi e/c) n_o V_o \left(\dot{V}_{yi} - \dot{V}_{ye}\right) \end{aligned} \tag{17}$$

Solving (10), (11), and (16), yields

$$\begin{aligned} \frac{V_{yi,e}}{V_o} &= \frac{B_o^2}{4\pi\rho_o V_o^2}\left(\frac{B_{xo}}{B_o}\frac{b_y}{B_o} + \frac{m_{e,i}c}{e_{e,i}B_o}\frac{\dot{b}_z}{B_o}\right) \\ \frac{V_{zi,e}}{V_o} &= \frac{B_o^2}{4\pi\rho_o V_o^2}\left(\frac{B_{xo}}{B_o}\frac{b_z}{B_o} - \frac{m_{e,i}c}{e_{e,i}B_o}\frac{\dot{b}_y}{B_o}\right) \end{aligned} \tag{18}$$

Using (18) to eliminate the $V_{y\alpha}$ and $V_{z\alpha}$ in (14) and (15) and then substituting the latter results into (17), the governing equation for the wave magnetic field can be obtained in a dimensionless form as

$$\frac{\ddot{b}_y^*}{M_{Ao}^2 \Omega_{io}^* \Omega_{eo}^*} = -\left\{\left[\frac{B_{xo}^{*2}}{M_{Ao}^2} - V_x^*(b_y^*, b_z^*)\right](B_{yo}^* + b_y^*) - \left[\frac{B_{xo}^{*2}}{M_{Ao}^2} - 1\right] B_{yo}^*\right\} - \left(\frac{1}{\Omega_{io}^*} - \frac{1}{\Omega_{eo}^*}\right)\frac{B_{xo}^*}{M_{Ao}^2}\dot{b}_z^* \tag{19}$$

$$\frac{\ddot{b}_z^*}{M_{Ao}^2 \Omega_{io}^* \Omega_{eo}^*} = -\left\{\left[\frac{B_{xo}^{*2}}{M_{Ao}^2} - V_x^*(b_y^*, b_z^*)\right] b_z^*\right\} + \left(\frac{1}{\Omega_{io}^*} - \frac{1}{\Omega_{eo}^*}\right)\frac{B_{xo}^*}{M_{Ao}^2}\dot{b}_y^* \tag{20}$$

where $M_{Ao} \equiv V_o/C_{Ao}$ and $C_{Ao} \equiv (B_o^2/4\pi\rho_o)^{1/2}$ are the upstream Alfvén Mach number, and Alfvén speed. The dimensionless quantities denoted by the superscript $*$ are normalized by a characteristic quantity on the upstream side. They are defined as $B_{xo}^* = B_{xo}/B_o = \cos\theta_o$, $B_{yo}^* = B_{yo}/B_o = \sin\theta_o$, $b_y^* = b_y/B_o$, $b_z^* = b_z/B_o$, $V_x^* = V_x/V_o$, $x^* = x/x_o$, $\tau^* = \tau\Omega_o$, $\dot{A}^* = dA^*/d\tau^* = V_x^* dA^*/dx^*$, $\ddot{A}^* = d^2A^*/d\tau^{*2}$, $\Omega_{io}^* = \Omega_{io}/\Omega_o$, and $\Omega_{eo}^* = \Omega_{eo}/\Omega_o$, where $\Omega_{io} \equiv eB_o/m_ic$ and $\Omega_{eo} \equiv eB_o/m_ec$ are the upstream ion and electron cyclotron frequencies, and $\Omega_o \equiv V_o/x_o$. The choice of the characteristic length x_o will be discussed later. The equation for $V_x^*(b_y^*, b_z^*)$ in (19) and (20) can be obtained from (9) in which p_i and p_e can be eliminated by (7). The resulting equation can be written as

$$V_x^* + \frac{\beta_o}{2M_{Ao}^2} V_x^{*-\gamma} + \frac{1}{2M_{Ao}^2}\left[\left(B_{yo}^* + b_y^*\right)^2 + b_z^{*2}\right] = 1 + \frac{\beta_o}{2M_{Ao}^2} + \frac{B_{yo}^{*2}}{2M_{Ao}^2} \tag{21}$$

where $\beta_o \equiv p_o/\left(B_o^2/8\pi\right)$ on the upstream side.

Multiplying m_α^2 to (13) and taking the difference between the resulting ion and electron equations, one obtains the wave electric field E_x, upon eliminating $\dot{p}_\alpha$, $V_{y\alpha}$, and $V_{z\alpha}$ by (7) and (18). The result can be written as

$$c^* E_x^*(b_y^*, b_z^*) = \frac{B_{xo}^* B_{yo}^* b_z^*}{M_{Ao}^2} + \left[\left(\frac{\dot{V}_x^*}{\Omega_{io}^*}\right) \Big/ \left(1 + \frac{T_{eo}}{T_{io}}\right)\right] \times \left[\left(1 - \frac{m_e}{m_i}\right) - \frac{\gamma\beta_o}{2M_{Ao}^2} \frac{1}{V_x^{*\gamma+1}} \left(1 - \frac{m_e}{m_i}\frac{T_{eo}}{T_{io}}\right)\right] \tag{22}$$

where $c^* \equiv c/V_o$, $E_x^* \equiv E_x/B_o$, and $T_{eo}/T_{io} = p_{eo}/p_{io}$ is the temperature ratio of electrons and ions on the upstream side. Both $V_x^*(b_y^*, b_z^*)$ and $\dot{V}_x^*(b_y^*, b_z^*)$ in (22) can be obtained from (21). By differentiating (21) once with respect to τ^* and solving $\dot{V}_x^*$, one obtains

$$\dot{V}_x^* = \frac{\dfrac{d}{d\tau^*}\left[\left(B_{yo}^* + b_y^*\right)^2 + b_z^{*2}\right]}{2M_{Ao}^2\left(\dfrac{\gamma\beta_o}{2M_{Ao}^2}\dfrac{1}{V_x^{*\gamma+1}} - 1\right)} \tag{23}$$

By introducing the local sound speed $C_S \equiv [\gamma(p_i + p_e)/(\rho_i + \rho_e)]^{1/2}$ and the local sound Mach number $M_S \equiv V_x/C_S$, it follows that

$$M_S = M_{Ao}\sqrt{2V_x^{*\gamma+1}/\gamma\beta_o} \tag{24}$$

When $M_S = 1$, the denominator in (23) vanishes. In this case, $\dot{V}_x^*$ can be solved by differentiating (21) twice with respect to τ^*, which yields

$$\dot{V}_x^* = \pm\sqrt{-\frac{d^2\left[\left(B_{yo}^* + b_y^*\right)^2 + b_z^{*2}\right]}{d\tau^{*2}} \times \frac{V_x^{*\gamma+2}}{\gamma(\gamma+1)\beta_o}} \tag{25}$$

where the sign is determined such that $\dot{V}_x^*$ is a continuous function. By introducing $B_\perp^* \equiv [(B_{yo}^* + b_y^*)^2 + b_z^{*2}]^{1/2}$, it can be seen that $\dot{V}_x^*$ remains finite at $M_S = 1$ if $B_\perp^*$ is a maximum at $M_S = 1$ (i.e., $\dot{B}_\perp^* = 0$ and $\ddot{B}_\perp^* < 0$). This is in contrast with previous claims [e.g., *Kakutani et al.*, 1967; *Crevier and Tidman*, 1970].

Equations (7), (8), (18)~(25) are the governing equations of nonlinear constant-profile waves. Equations (19), (20) and (23) can be solved numerically for $\mathbf{b}(x)$, $\dot{\mathbf{b}}(x)$ and $V_x(x)$ when $M_S \neq 1$. The results can be substituted into (7), (8), (18) and (22) for the remaining variables $p_\alpha(x)$, $\rho(x)$, $V_{y\alpha}(x)$, $V_{z\alpha}(x)$ and $E_x(x)$. When M_S approaches 1, (23) must be replaced by (25). However, (25) is difficult to handle numerically. This difficulty can be overcome by the "pseudo potential method" discussed below.

According to the pseudo potential method [e.g., *Davis et al.*, 1958; *Montgomery*, 1959; *Hain et al.*, 1960; *Sagdeev*, 1966; *Crevier and Tidman*, 1970], (19) and (20) can be viewed as the "equations of motion" of a "fictitious particle". The "coordinate" of the "fictitious particle" is the wave magnetic field $\mathbf{b}$. One can define a "velocity" ($\dot{\mathbf{b}}$) independent pseudo potential Ψ, such that the "equations of motion" (19) and (20) can be rewritten as

$$\frac{\ddot{b}_y^*}{M_{Ao}^2\Omega_{io}^*\Omega_{eo}^*} = -\frac{\partial\Psi(b_y^*, b_z^*)}{\partial b_y^*} - \left(\frac{1}{\Omega_{io}^*} - \frac{1}{\Omega_{eo}^*}\right)\frac{B_{xo}^*}{M_{Ao}^2}\dot{b}_z^* \tag{26}$$

$$\frac{\ddot{b}_z^*}{M_{Ao}^2\Omega_{io}^*\Omega_{eo}^*} = -\frac{\partial\Psi(b_y^*, b_z^*)}{\partial b_z^*} + \left(\frac{1}{\Omega_{io}^*} - \frac{1}{\Omega_{eo}^*}\right)\frac{B_{xo}^*}{M_{Ao}^2}\dot{b}_y^* \tag{27}$$

where Ψ is defined by

$$\frac{\partial\Psi(b_y^*, b_z^*)}{\partial b_y^*} \equiv \left[\frac{B_{xo}^{*2}}{M_{Ao}^2} - V_x^*(b_y^*, b_z^*)\right]\left(B_{yo}^* + b_y^*\right) - \left[\frac{B_{xo}^{*2}}{M_{Ao}^2} - 1\right]B_{yo}^* \tag{28}$$

$$\frac{\partial\Psi(b_y^*, b_z^*)}{\partial b_z^*} \equiv \left[\frac{B_{xo}^{*2}}{M_{Ao}^2} - V_x^*(b_y^*, b_z^*)\right] b_z^* \tag{29}$$

The function Ψ is a legitimate potential function, since the partial differentiation of (28) with respect to b_z^* is identical to the partial differentiation of (29) with respect to b_y^*. The analytic form of the pseudo potential

$\Psi(b_y^*, b_z^*)$ can be obtained by the following procedures [e.g., *Hain et al.*, 1960; *Crevier and Tidman*, 1970].

Multiplying (26) by $\dot{b}_y^*$, (27) by $\dot{b}_z^*$, and adding the resulting equations, one obtains an equation which can be integrated once and written as

$$\frac{1}{2}\frac{\dot{b}_y^{*2}+\dot{b}_z^{*2}}{M_{Ao}^2\Omega_{io}^*\Omega_{eo}^*}+\Psi(b_y^*,b_z^*)=0 \tag{30}$$

where $\Psi = 0$ has been chosen on the upstream side. By using (18) to eliminate $V_{y\alpha}$, $V_{z\alpha}$ and using (7) to eliminate p_i, p_e, the conservation of energy flux in (12) can be rewritten in a dimensionless form:

$$\frac{M_{Ao}^2}{2}V_x^{*2}+\frac{5\beta_o}{4}V_x^{*1-\gamma}+B_{yo}^*(B_{yo}^*+b_y^*)$$

$$+\frac{B_{xo}^{*2}}{2M_{Ao}^2}\left(b_y^{*2}+b_z^{*2}\right)+\frac{1}{2}\frac{\dot{b}_y^{*2}+\dot{b}_z^{*2}}{M_{Ao}^2\Omega_{io}^*\Omega_{eo}^*}$$

$$=\frac{M_{Ao}^2}{2}+\frac{5\beta_o}{4}+B_{yo}^{*2} \tag{31}$$

Comparing (30) and (31), the pseudo potential $\Psi(b_y^*, b_z^*)$ can be written as

$$\Psi(b_y^*,b_z^*)\equiv\frac{M_{Ao}^2}{2}\left\{\left[V_x^*(b_y^*,b_z^*)\right]^2-1\right\}$$

$$+\frac{5\beta_o}{4}\left\{\left[V_x^*(b_y^*,b_z^*)\right]^{1-\gamma}-1\right\}$$

$$+B_{yo}^*b_y^*+\frac{B_{xo}^{*2}}{2M_{Ao}^2}\left(b_y^{*2}+b_z^{*2}\right) \tag{32}$$

where the equation for $V_x^*(b_y^*, b_z^*)$ is given by (21).

3. Analytic Solutions

3.1. *General Solution Behavior*

The magnetic field and density of nonlinear wave solutions can be examined using the pseudo potential method. The main results are summarized as follows. (1) The magnetic field variation of nonlinear Alfvénic fluctuations follows closely the equipotential contour of Ψ and the polarization of the magnetic field is governed by the gradient of Ψ, when $M_{Ao} \ll \cos\theta_o(m_i/m_e)^{1/2}$. (2) The density $\rho(x)$ and the total magnetic field $B(x)$ are in phase when $M_S > 1$ but out of phase when $M_S < 1$. These results are obtained by the following procedure.

The vector form of the equations of motion in (26) and (27) can be written as

$$C_1\ddot{\mathbf{b}}^*=-\nabla_{\mathbf{b}^*}\Psi+C_2B_{xo}^*\hat{\mathbf{x}}\times\dot{\mathbf{b}}^* \tag{33}$$

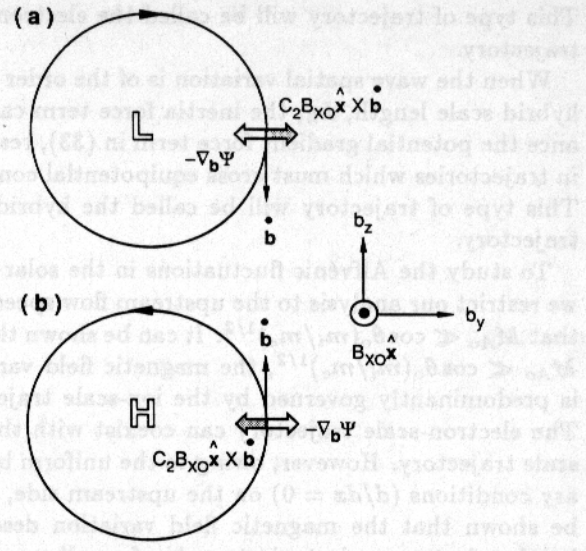

Fig. 1. Illustrating of the force balance of the ion-scale trajectory which is characterized by the motion along equipotential contours. The magnetic field polarization has to be (*a*) left-handed when the equipotential contour curves around a low potential center, and (*b*) right-handed when the equipotential contour curves around a high potential center, so that the velocity dependent force term $(C_2B_{xo}^*\hat{\mathbf{x}}\times\dot{\mathbf{b}}^*)$ can balance the potential gradient force term $(-\nabla_{\mathbf{b}^*}\Psi)$ in (33).

where $C_1 = 1/M_{Ao}^2\Omega_{io}^*\Omega_{eo}^*$, $C_2 = (\Omega_{eo}^* - \Omega_{io}^*)/M_{Ao}^2\Omega_{io}^*\Omega_{eo}^*$ and $\nabla_{\mathbf{b}^*} = \hat{\mathbf{y}}\partial/\partial b_y^* + \hat{\mathbf{z}}\partial/\partial b_z^*$. For convenience, we define $L_i = C_{Ao}\cos\theta_o/\Omega_{io}M_{Ao}$ as an ion scale length, $L_e = V_o/\Omega_{eo}\cos\theta_o$ as an electron scale length, and $L_h = (L_iL_e)^{1/2} = C_{Ao}/(\Omega_{io}\Omega_{eo})^{1/2}$ as a hybrid scale length, so that the motion of the "fictitious particle" can be classified into three simple forms based on the three scale lengths.

When the wave spatial variation is of the order of the ion scale length, L_i, or longer, the "inertia force" term $(C_1\ddot{\mathbf{b}}^*)$ in (33) is negligible. The balance between the "potential gradient force" term $(-\nabla_{\mathbf{b}^*}\Psi)$ and the "velocity dependent force" term $(C_2B_{xo}^*\hat{\mathbf{x}}\times\dot{\mathbf{b}}^*)$ results in a "motion along equipotential contours." This type of trajectory will be called the ion-scale trajectory. The magnetic field polarization associated with the ion-scale trajectory is illustrated in Figure 1. As can be seen in Figure 1, the polarization with respect to $\hat{\mathbf{x}}B_{xo}$ have to be (1*a*) left-handed when the equipotential contour bends around a low potential center, and (1*b*) right-handed when the contour bends around a high potential center, so that the "velocity dependent force" $(C_2B_{xo}^*\hat{\mathbf{x}}\times\dot{\mathbf{b}}^*)$ can balance the "potential gradient force" $(-\nabla_{\mathbf{b}^*}\Psi)$ in (33).

When the wave spatial variation is of the order of the electron scale length, L_e, the "inertia force" term will be large enough to balance the "velocity dependent force" term in (33), resulting in a right-handed "gyromotion."

This type of trajectory will be called the electron-scale trajectory.

When the wave spatial variation is of the order of the hybrid scale length, L_h, the inertia force term can balance the potential gradient force term in (33), resulting in trajectories which must cross equipotential contours. This type of trajectory will be called the hybrid-scale trajectory.

To study the Alfvénic fluctuations in the solar wind, we restrict our analysis to the upstream flow speed such that $M_{Ao} \ll \cos\theta_o(m_i/m_e)^{1/2}$. It can be shown that for $M_{Ao} \ll \cos\theta_o(m_i/m_e)^{1/2}$, the magnetic field variation is predominantly governed by the ion-scale trajectory. The electron-scale trajectory can coexist with the ion-scale trajectory. However, owing to the uniform boundary conditions ($d/dx = 0$) on the upstream side, it can be shown that the magnetic field variation described by the electron-scale trajectory is of small amplitude compared with B_o ($\delta b \sim B_o m_e/m_i$). If the "potential gradient force" along the equipotential contour is nonuniform, the trajectory cannot follow the equipotential contours exactly. The trajectory will deviate slightly from the equipotential contour (i.e., the hybrid-scale trajectory) and shift toward the low potential side by an amount $\delta b \sim B_o(m_e/m_i)^{1/2}$. Hence, the magnetic field variation of the nonlinear Alfvénic fluctuations is strongly guided by the equipotential contour of Ψ and the polarization of the magnetic field is governed by the gradient of Ψ. However, care must be taken in evaluating the equipotential contours of Ψ from (32), because V_x^* is a double value function of (b_y^*, b_z^*), so that Ψ is also a double value function of (b_y^*, b_z^*) [e.g., *Crevier and Tidman*, 1970].

Figure 2 shows the double value nature of V_x^* at $b_z^* = 0$, where Z indicates $B_\perp^* = 0$ (i.e., $b_y^* = -B_{yo}^*$, $b_z^* = 0$). Points X and Y divide the closed curve into two parts: the solid curve and the dashed curve, each of them is a single value function of b_y^*. The characteristics of these two curves can be obtained by differentiating (21) once with respect to b_y^*, i.e.,

$$\frac{\partial V_x^*}{\partial b_y^*} = \frac{B_{yo}^* + b_y^*}{M_{Ao}^2} \Big/ \left(\frac{1}{M_S^2} - 1\right) \tag{34}$$

where M_S is given in (24). According to (34) $\partial V_x^*/\partial b_y^* \to \infty$ as $M_S \to 1$, while $\partial V_x^*/\partial b_y^* \to \infty$ at X and Y as can be seen in Figure 2. Thus, $M_S = 1$ at X and Y which will be called the sonic points. Moreover, M_S increases with increasing V_x^* according to (24). Hence, the solid curve is the supersonic curve ($M_S > 1$), and the dashed curve is the subsonic curve ($M_S < 1$). The above discussion of the double value nature is equally applicable to the entire b_y^*-b_z^* space. Therefore, the contour of Ψ or V_x^* must be evaluated separately for $M_S \geq 1$ and $M_S \leq 1$.

The density variation of the waves can be obtained from the constant V_x^* contours as discussed below.

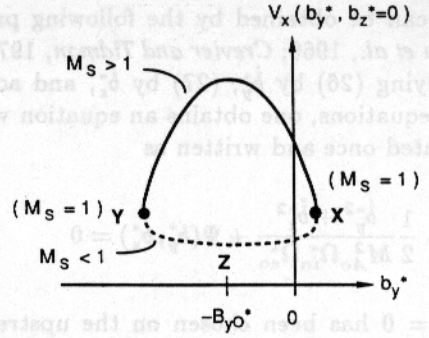

Fig. 2. Plot of the cross-section of function $V_x^*(b_y^*, b_z^*)$ at $b_z^* = 0$. Since the constant $V_x^*(b_y^*, b_z^*)$ contours are circles centered at $B_\perp^* = 0$, this cross-section diagram infers that $V_x(x)$ and $B_\perp(x)$ are out of phase when $M_S > 1$ and in phase when $M_S < 1$.

From (21), it follows that the constant V_x^* contours are circles centered at Z where $B_\perp^* = 0$. Since Figure 2 represents a typical configuration for the cross section of V_x^* at $b_z^* = 0$, it follows that V_x^* increases monotonically toward Z on the supersonic surface ($M_S > 1$) but decreases monotonically toward Z on the subsonic surface ($M_S < 1$). Hence, $V_x(x)$ and $B_\perp(x)$ are out of phase on the supersonic surface but in phase on the subsonic surface. According to (8), the variations of ρ and V_x are out of phase. Combing the relationship between $B_\perp$, V_x and ρ, it follows that the density $\rho(x)$ and the total magnetic field $B(x) \equiv (B_\perp^2 + B_{xo}^2)^{1/2}$ are in phase on the supersonic surface, but out of phase on the subsonic surface.

3.2. *Wave Trains and Solitons*

The nonlinear wave solutions will be discussed based on the upstream flow speed V_o relative to the upstream slow-mode speed (V_{SLo}), Alfvén-mode speed ($V_{AXo} \equiv C_{Ao}\cos\theta_o$), fast-mode speed ($V_{Fo}$) and the sound speed ($C_{So}$), where V_{Fo} and V_{SLo} are defined by

$$\frac{V_{Fo}}{V_{SLo}} = \left[\frac{1}{2}\left(C_{So}^2 + C_{Ao}^2 \pm \sqrt{(C_{So}^2 + C_{Ao}^2)^2 - 4C_{So}^2 V_{AXo}^2}\right)\right]^{1/2}$$

Figure 3 shows the structure of Ψ. The upper two diagrams sketch the three-dimensional structures of $\Psi(b_y^*, b_z^*)$ for two different ranges of the upstream flow speed as indicated. The lower six diagrams of Figure 3 show the cross sections of Ψ at $b_z^* = 0$, where (*a1*), (*b1*) are for $V_o = V_{AXo}$; (*a2*), (*b2*) are for V_o slightly less than V_{AXo}; and (*a3*), (*b3*) are for V_o slightly greater than V_{AXo}. The points X, Y and Z in this figure are the same as defined in Figure 2. Point A is the "upstream point" in which $V_x^* = 1$ and $b_y^* = b_z^* = 0$. From (28) and (29), it can be shown that the upstream point A is a

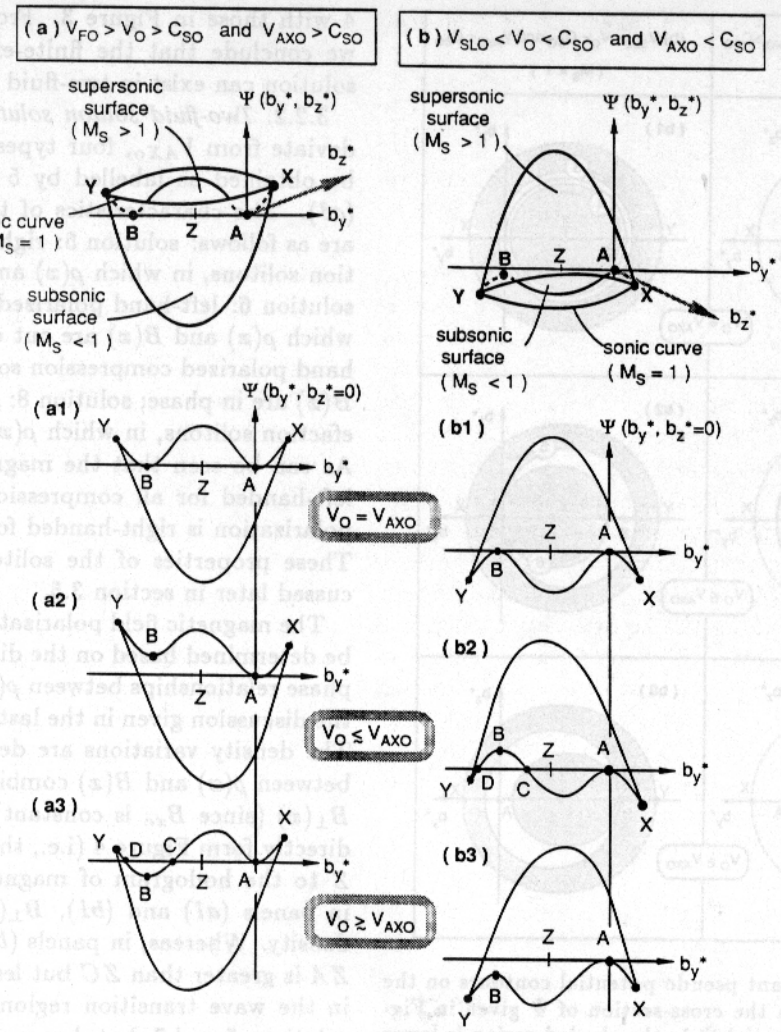

Fig. 3. Sketches of the structure of the pseudo potential Ψ. The upper two diagrams show the three-dimensional structures of $\Psi(b_y^*, b_z^*)$ for different plasma temperature and upstream flow speed as indicated. The lowers six diagrams show the cross-section of Ψ when V_o is around V_{AXo}. The point A is the upstream point in which $\Psi = 0$, $V_x^* = 1$ and $b_y^* = b_z^* = 0$.

flat point at which $\partial\Psi/\partial b_y^* = \partial\Psi/\partial b_z^* = 0$. The pseudo potential Ψ consists of a supersonic surface ($M_S > 1$) and a subsonic surface ($M_S < 1$). The supersonic surface always lies above the subsonic surface. The two surfaces meet at the sonic curve ($M_S = 1$). Form the lower six diagrams, it can be seen that the Ψ tilts up (down) on the side of Y when V_o is less (greater) than V_{AXo}, but sits upright when $V_o = V_{AXo}$.

For convenience, we define the surface containing the upstream point A as the "upstream surface." Figure 4 illustrates the equipotential contours on the upstream surface of the six cases given in Figure 3. The points A, B, C, D, X, Y, and Z in Figure 4 correspond to the points shown in Figure 3. The dashed circle is the sonic circle ($M_S = 1$) centered at Z. The potential Ψ in the shaded region is lower than in the blank region. It can be seen that the $\Psi = 0$ contour is a circle passing though points A and B when $V_o = V_{AXo}$, but split into two loops when V_o slightly deviate from V_{AXo}. The upstream point A in Figure 4 is a saddle point in panels (*b2*) and (*a3*), a minimum point in panel (*a2*), and a maximum point in panel (*b3*).

According to the uniform boundary condition and the discussion in section 3.1, for cases of $M_{Ao} \ll \cos\theta_o(m_i/m_e)^{1/2}$, the magnetic field hodogram of the wave solution must start from the upstream point A, and follow closely the equipotential contour $\Psi = 0$. The solutions associated with the equipotential contours in Figure 4 are described below.

3.2.1. *Oblique wave train solutions.* When $V_o = V_{AXo}$, nonlinear oblique Alfvén wave train solutions exist as labelled by $1 \sim 4$ in panels (*a1*) and (*b1*) of Figure 4. These wave train solutions are characterized by constant density and circular polarization. Their wave length are at least two orders of magnitude greater than the ion gyroradius. This means that these waves exist only in the MHD limit. The arrows in Figure 4 indicate the polarization directions for $B_{xo} > 0$. The

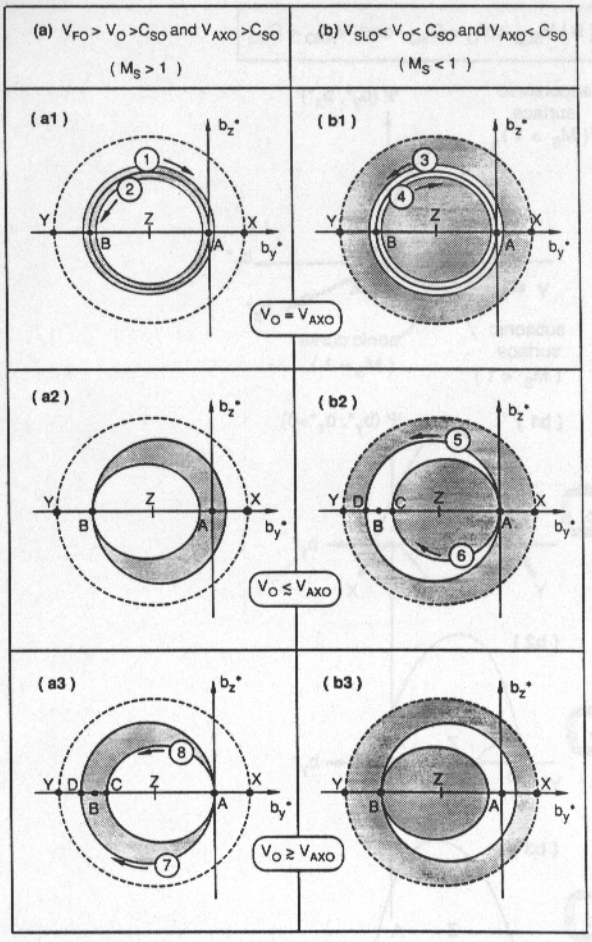

Fig. 4. Plots of constant pseudo potential contours on the upstream surfaces with the cross-section of Ψ given in Figure 3. The pseudo potential Ψ in the shaded region is lower than in the blank region. The dashed circle is the sonic circle where $M_S = 1$. The contour plots are used to obtain the magnetic field hodogram of the nonlinear wave solutions, which must start from the upstream point A, and follow closely the equipotential contour $\Psi = 0$. The magnetic field hodogram of the MHD wave train solutions $1 \sim 4$ and the two-fluid soliton solutions $5 \sim 8$ are obtained and labelled in panels (*a1*), (*b1*), (*b2*), and (*a3*). The polarization direction of each solution is denoted by arrow for $B_{xo} > 0$. Characteristics of the solutions are given in section 3.2. The solution 6 will be identified as the slow soliton, the solution 8 will be identified as the fast soliton, the solution 5 and 7 will be identified as the Alfvén solitons in section 4. No nonlinear wave solutions are found in panels (*a2*) and (*b3*). The $B_{xo} > 0$ has been assumed in plotting the arrow of each solution.

polarization is left-handed in solutions 1 and 4, but is right-handed in solutions 2 and 3.

The wave train solutions $1 \sim 4$ can be of finite extent if required by the boundary condition. This can occur because the equipotential contour for solutions $1 \sim 4$ is on a "flat" circle passing through A and B in panels (*a1*) and (*b1*) of Figure 4. The flate nature of the contour can be seen by comparing panels (*a1*) and (*b1*) in Figure 4 with those in Figure 3. From the above discussion, we conclude that the finite-extent Alfvén wave train solution can exist in two-fluid plasmas.

3.2.2. *Two-fluid soliton solutions.* When V_o slightly deviate from V_{AXo}, four types of soliton solutions can be obtained as labelled by $5 \sim 8$ in panels (*b2*) and (*a3*). The characteristics of the four soliton solutions are as follows: solution 5: right-hand polarized rarefaction solitons, in which $\rho(x)$ and $B(x)$ are out of phase; solution 6: left-hand polarized compression solitons, in which $\rho(x)$ and $B(x)$ are out of phase; solution 7: left-hand polarized compression solitons, in which $\rho(x)$ and $B(x)$ are in phase; solution 8: right-hand polarized rarefaction solitons, in which $\rho(x)$ and $B(x)$ are in phase. As can be seen that the magnetic field polarization is left-handed for all compression solitons; whereas, the polarization is right-handed for all rarefaction solitons. These properties of the soliton solutions will be discussed later in section 3.5.

The magnetic field polarization in solutions $1 \sim 8$ can be determined based on the discussion of Figure 1. The phase relationships between $\rho(x)$ and $B(x)$ follows from the discussion given in the last paragraph of section 3.1. The density variations are determined by the relation between $\rho(x)$ and $B(x)$ combined with the variation of $B_\perp(x)$ (since B_{xo} is constant), which can be obtained directly form Figure 4 (i.e., the distance from the point Z to the hodogram of magnetic field). For example, in panels (*a1*) and (*b1*), $B_\perp(x)$ is constant, so is the density. Whereas, in panels (*b2*) and (*a3*), the distance ZA is greater than ZC but less than ZD, so that $B(x)$ in the wave transition region increases for outer loop solutions 5 and 7, but decreases for inner loop solutions 6 and 8. The spatial profiles, $\rho(x)$, $B(x)$, $\phi(x)$, $b_y(x)$, and $b_z(x)$, of the solutions $1 \sim 8$ are sketched in Figure 5, qualitatively, where ϕ is the phase angle defined by $\tan^{-1}(B_z/B_y)$. A numerical result will be presented in section 4 for a comparison with observations.

No large amplitude isentropic wave solutions can exist when V_o is in between V_{AXo} and C_{So}, as shown in panels (*a2*) and (*b3*) of Figure 4. Because in these two cases, the equipotential contour passing through the upstream point A reduces to A itself, so that the "fictitious particle" can only gyrate around A in small amplitude ($\delta b \sim B_o m_e/m_i$). Similar results can be obtained when $V_o < V_{SLo}$ (for which the point A is a minimum point) and $V_o > V_{Fo}$ (for which the point A is a maximum point, see *Crevier and Tidman* [1970]) as long as the condition of $M_{Ao} \ll \cos\theta_o (m_i/m_e)^{1/2}$ is satisfied.

3.3. *Two-Fluid Rotational Discontinuity*

As V_o deviates further from V_{AXo}, the outer loop in panels (*b2*) and (*a3*) of Figure 4 may intersect with the sonic circle. In these cases, the soliton solution associated with the outer loop will turn into a rotational structure, which is called the two-fluid rotational discontinuity.

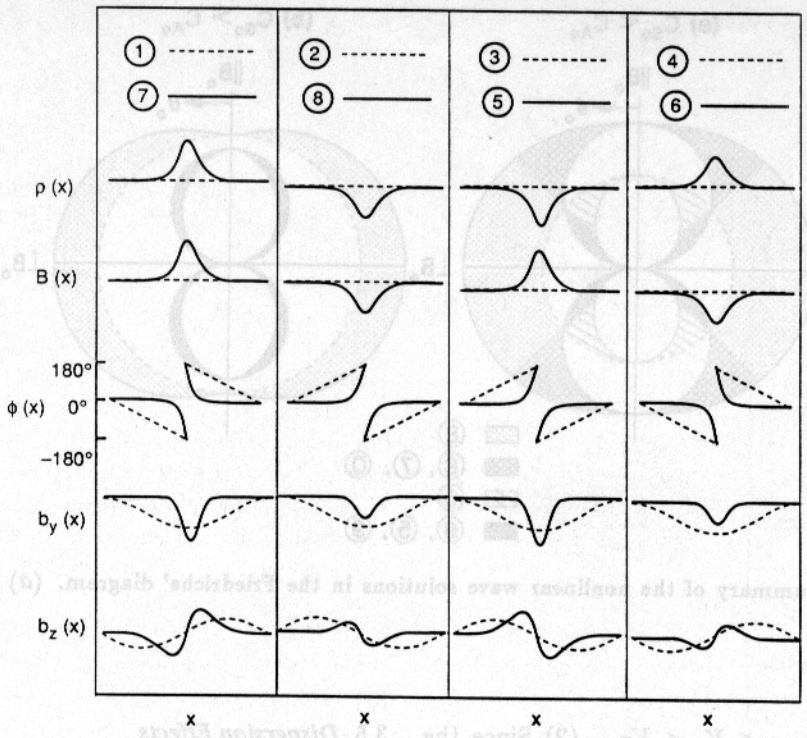

Fig. 5. Sketches of the spatial profiles for the nonlinear solutions $1 \sim 8$, in which B_{xo} is assumed to be positive.

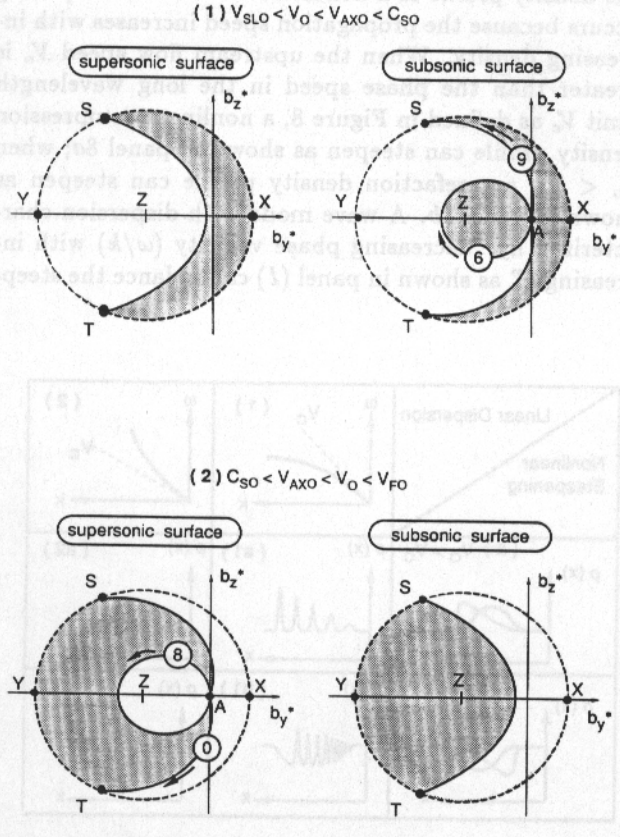

Fig. 6. Examples of the two-fluid rotational discontinuity solutions 9 and 0, where B_{xo} is assumed to be positive.

Figure 6 illustrates two cases in which the two-fluid rotational discontinuity solutions exist as labeled by 9, and 0. Points S and T in Figure 6 are the intersections of the outer loop of $\Psi = 0$ contours on the sonic circle. B_{xo} is assumed to be positive in both cases.

Solution 9 in Figure 6 starts from A and ends at S if $V_{SLo} < V_o < V_{AXo} < C_{So}$. The characteristics of solution 9 are similar to that of the soliton solution 5 but with rotation angle no more than 180°. The maximum rotation angle (180°) is obtained based on the fact that Ψ is symmetric to the b_y^* axis, so are the locations of points S and T. Likewise, if $C_{So} < V_{AXo} < V_o < V_{Fo}$, the solution 0 in Figure 6 starts from A and ends at T with characteristics similar to the soliton solution 7 but with rotation angle no more than 180°. To shown that the points S and T are legitimate downstream points, one needs to show that: (1) they are the trapping points, namely, the "fictitious particle" cannot continue its trip by going through the $\Psi = 0$ contour on the other surface and then return to the upstream point A; (2) the $\dot{V}_x$ is of finite when $M_S = 1$. Demonstrations of these two remarks are given as follows. (1) It is seen that both ST and AS curve around high potential center in the case of $V_{SLo} < V_o < V_{AXo} < C_{So}$ in Figure 6. According to the discussion of Figure 1, the "fictitious particle" moving from A to S will be trapped at the point S with a small amplitude gyration ($\delta b \sim B_o m_e/m_i$) on the downstream side. Likewise, it can be shown that the "fictitious particle" will be trapped at point T in

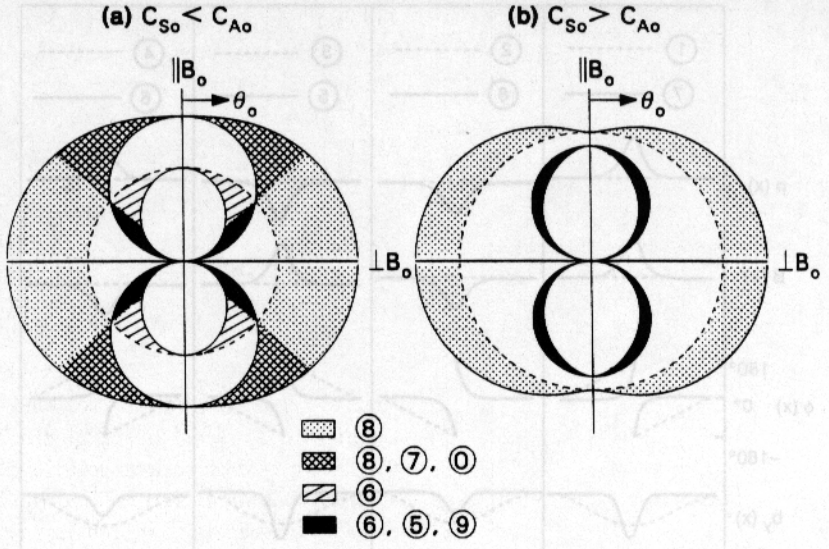

Fig. 7. The summary of the nonlinear wave solutions in the Friedrichs' diagram. (*a*) $\beta_o = 0.5$; (*b*) $\beta_o = 1.8$.

the case of $C_{So} < V_{AXo} < V_o < V_{Fo}$. (2) Since the sonic circle is the outer boundary of Ψ and is centered at Z where $B_\perp^* = 0$, so that $B_\perp^*$ is maximum at the sonic circle. It follows that $B_\perp^*(x)$ is a maximum in the wave transition region when the flow speed is equal to the local sound speed. Hence, based on the discussion of (23)~(25), the $\dot{V}_x^*$ remains finite as $M_S = 1$. This is in contrast with the previous studies [e.g., *Kakutani et al.*, 1967; *Crevier and Tidman*, 1970] in which the solution is believed to diverge on the sonic curve due to the incorrect conclusion that $\dot{V}_x^* \to \infty$ at $M_S \to 1$. It may be noted that the dispersion effect when $M_S \to 1$, in the formation of the two-fluid rotational discontinuity will be discussed later in section 3.5 in detail.

3.4. *Summary of Solutions on the Friedrichs' Diagram*

Figure 7 summarizes the solutions in the Friedrichs' diagram [e.g., *Kantrowitz and Petschek*, 1966] for V_o less than V_{Fo}, to show the dependence of the nonlinear waves on θ_o, M_{Ao} and β_o, where (*a*) is for $C_{So} < C_{Ao}$ and (*b*) is for $C_{So} > C_{Ao}$. The radius of the polar plot indicates the upstream flow velocity $V_o\hat{\mathbf{x}}$. The polar angle θ_o is measured from the vertical axis which is parallel to the upstream magnetic field ($\mathbf{B}_o$). The nonlinear isentropic wave solutions exist in the shaded regions as indicated by the legends. No isentropic nonlinear wave solutions have been found in the blank regions. The solutions on the curves of the fast-mode, slow-mode, and sound speeds are described as follows. The amplitude of the inner loop solution 6 or 8 vanishes when $V_o = V_{Fo}$ or $V_o = V_{SLo}$, respectively, whereas the outer loop solutions 5, 7, 9, or 0 may still be of finite amplitude. On the other hand, when $V_o = C_{So}$, the outer loop solutions vanish but the inner loop solutions may still be of finite amplitude.

3.5. *Dispersion Effects*

The formation of solitons is known to depend on the balance between the nonlinear steepening and the wave dispersion. Figure 8 shows the relationship between the nonlinear steepening and the linear dispersion on the density profile of a nonlinear wave. The steepening occurs because the propagation speed increases with increasing density. When the upstream flow speed V_o is greater than the phase speed in the long wavelength limit V_c as defined in Figure 8, a nonlinear compression density profile can steepen as shown in panel 8*a*; when $V_o < V_c$, a rarefaction density profile can steepen as shown in panel 8*b*. A wave mode with dispersion characterized by "decreasing phase velocity (ω/k) with increasing k" as shown in panel (*1*) can balance the steep-

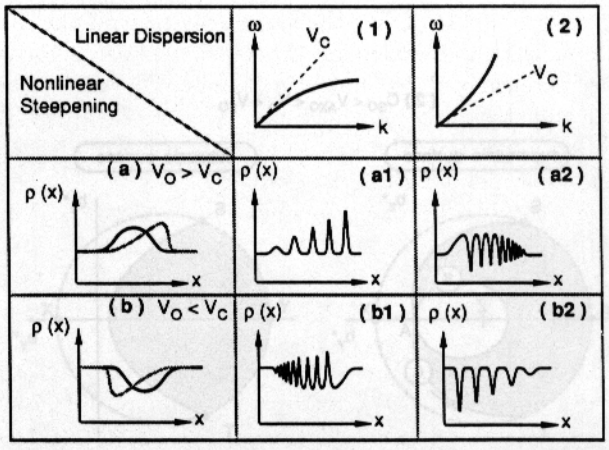

Fig. 8. Illustrating of the balance between the nonlinear steepening and the dispersion effects for a finite amplitude compression or rarefaction density profile.

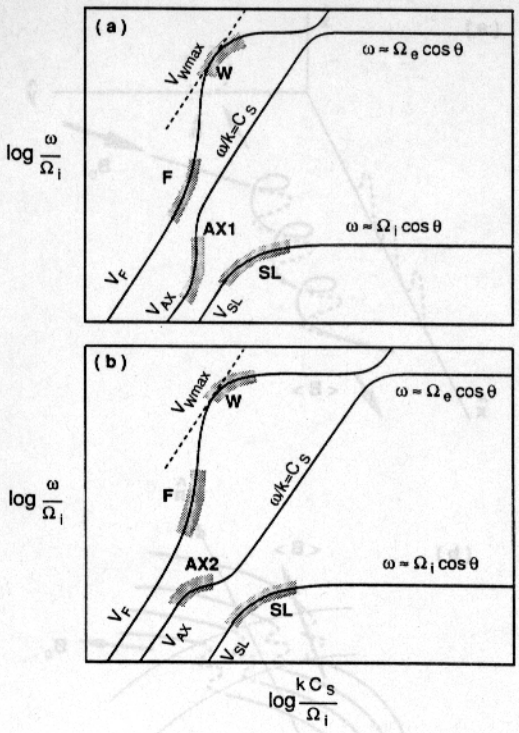

W RH Polarized / compression soliton as $V_o > V_{wmax}$ / Whistler soliton

F RH Polarized / rarefaction soliton as $V_o < V_F$ / soliton solution (8)

AX1 RH Polarized / rarefaction soliton as $V_o < V_{AX1}$ / soliton solution (5)

AX2 LH Polarized /compression soliton as $V_o > V_{AX2}$ / soliton solution (7)

SL LH Polarized / compression soliton as $V_o > V_{SL}$ / soliton solution (6)

Fig. 9. Sketches of two-fluid linear wave dispersion relation for obliquely propagating waves. (*a*) $C_S > V_{AX}$; (*b*) $C_S < V_{AX}$ (followed after *Stringer* [1963]; *Formisano and Kennel* [1969]).

ening of the compression density profile to form a series of compression solitons as shown in panel (*a1*); but no solitons can form for the rarefaction density profile, as shown in panel (*b1*). By the same argument, if the dispersion is characterized by "increasing phase velocity with increasing k" as shown in panel (*2*), a rarefaction wave will steepen to form a series of rarefaction solitons as shown in panel (*b2*); but no solitons can form for the compression density profile, as shown in panel (*a2*).

Figure 9 sketches the two-fluid linear wave dispersion relation for oblique propagation, where 9*a* is for $C_S > V_{AX}$ and 9*b* is for $C_S < V_{AX}$ [*Stringer*, 1963; *Formisano and Kennel*, 1969]. The dispersion effect on the shaded segments will be shown to be related to the formation of two-fluid solitons.

The dispersion characteristics depend on the magnetic field polarization as has been shown by *Stringer* [1963] and *Formisano and Kennel* [1969]. When the wave length approaches the ion scale length, $\omega/k\Omega_{io}\cos\theta$, the left-hand polarized wave will slow down due to increasing ion inertia loading; whereas, the right-hand polarized wave will speed up due to decreasing ion inertia loading. Likewise, when the wave length approaches the electron scale length, $\omega/k\Omega_{eo}\cos\theta$, the right-hand polarized wave will slow down due to increasing electron inertia loading [*Stringer*, 1963; *Formisano and Kennel*, 1969]. Hence, the dispersion in the shaded segments SL and $AX2$ are associated with left-hand polarized waves; the dispersion in $AX1$, F and W are related to right-hand polarized waves, as shown in the legends of Figure 9.

The soliton solutions associated with the shaded segments are indicated in the legends of Figure 9. The results are obtained based on the discussion in Figure 8 that compression soliton solutions exist if ω/k decreases with increasing k, and rarefaction soliton solutions exist if ω/k increases with increasing k. As can be seen in the legends of Figure 9, for dispersion in the ion-scale length (i.e., in SL, $AX1$, $AX2$, and F) the magnetic field polarization is left-handed for the compression solitons, and right-handed for the rarefaction solitons.

The soliton solutions 5, 6, 7, and 8 in Figure 4 can be associated with the dispersions denoted by $AX1$, SL, $AX2$ and F in Figure 9, respectively. Likewise, the whistler soliton solution [e.g., *Kellogg*, 1964; *Kakutani et al.*, 1967] can be associated with the dispersion in segment W. Based on the above association, the soliton solution 6 can be called the "slow-mode soliton" as V_o decreases toward V_{SLo}, and the soliton solution 8 can be called the "fast-mode soliton" as V_o increases toward V_{Fo}. Similar results can be obtained by the Korteweg-deVries (KdV) equation for V_o slightly greater than V_{SLo} or V_o slightly less than V_{Fo} [e.g., *Churilov*, 1980; *Kennel et al.*, 1988]. Note that the fast-mode and slow-mode solitons can evolve into the Alfvén wave train solutions 2 and 4, respectively, as $V_o \rightarrow V_{AXo}$. The evolution takes place due to the increasing influence of the Alfvén-mode dispersion as $V_o \rightarrow V_{AXo}$. The soliton solutions 5 and 7 can exist only when V_o deviates slightly from V_{AXo}, and therefore can be called the "Alfvén-mode solitons." Similar results can be obtained by the modified Korteweg-deVries (MKdV) equation [e.g., *Churilov*, 1980; *Kennel et al.*, 1988].

It has been shown in Figure 6 that the Alfvén-mode solitons 5 and 7 turn into the two-fluid rotational discontinuities 9 and 0 as V_o further deviated from V_{AXo}. The formation of the rotational discontinuities 9 and 0 is due to the conversion of the Alfvén mode into the electrostatic ion acoustic mode [*Stringer*, 1963] when the phase speed approaches the sound speed as can be seen in Figure 9. Thus, the magnetic field of the two-fluid rotational discontinuity stop rotating as $M_S \rightarrow 1$.

4. Comparison With Observations

In this section, the rotational discontinuity solutions, wave train solutions, and soliton solutions obtained in

Section 3, will be compared with the characteristics of Alfvénic fluctuations observed in the solar wind.

4.1. *Rotational Discontinuity*

The thickness of the observed rotational discontinuity in the solar wind is found to be a few tens of ion gyroradii [e.g., *Martin et al.*, 1973; *Burlaga et al.*, 1977; *Lepping and Behannon*, 1986]. The density fluctuations observed in the rotational discontinuity can contribute to the humped spectrum [*Unti and Russell*, 1976]. The rate of magnetic field rotation across the discontinuity is observed to be variable as shown in Figure 2 of *Lepping and Behannon* [1986].

According to the pseudo potential structure shown in section 3, rotational discontinuities (R-D) can be classified into (a) the MHD rotational discontinuity and the two-fluid rotational discontinuity as discussed below:

The MHD R-D is characterized by a constant angular rotation rate, with $V_o = V_{AXo}$ and a total rotation angle less than 360°. The thickness is of $\sim 10^2$ to $\sim 10^3$ times the ion gyroradii which is much greater than the thickness of the rotational discontinuity observed at the magnetopause and in the solar wind.

The two-fluid R-D is given by 9 and 0 in Figure 6, in which $V_o \neq V_{AXo}$ and the total angle of rotation must be less than 180° which is consistent with observations [e.g., *Sonnerup and Cahill*, 1968; *Berchem and Russell*, 1982*b*] and simulation results [*Swift and Lee*, 1983]. The rate of angular rotation increases toward the downstream side. The thickness ranges from ~10 to ~100 times the ion gyroradii, depending on the β_o, θ_o, and M_{Ao}, which is consistent with observations in the solar wind [e.g., *Martin et al.*, 1973; *Burlaga et al.*, 1977; *Lepping and Behannon*, 1986] and at the magnetopause [e.g., *Berchem and Russell*, 1982*a*]. The density fluctuation in the two-fluid R-D is a consequence of the ion inertial effect which is believed to contribute to the humped spectrum of magnetic field [*Unti and Russell*, 1976].

4.2. *Identification of Nonlinear Alfvénic Fluctuations With Finite-Extent Alfvén Wave Train Solutions*

Observations show that the wave normal, $\hat{\mathbf{n}}$, of the Alfvénic fluctuations is highly parallel to the local average magnetic field, $\langle \mathbf{B} \rangle$, with a half-width deviation of $20° \sim 30°$ [e.g., *Belcher and Davis*, 1971; *Daily*, 1973; *Solodyna and Belcher*, 1976; *Denskat and Neubauer*, 1982]. This observed feature of the Alfvénic fluctuation can be understood in terms of nonlinear wave solutions as discussed below.

From the magnetic field hodogram of $1 \sim 8$ shown in Figure 4, the center of the hodogram is around the point Z at which $B_\perp = 0$, i.e., the average $\mathbf{B}_\perp$ $(\equiv \hat{\mathbf{y}}(B_{yo} + b_y) + \hat{\mathbf{z}} b_z)$ in the wave transition region nearly vanishes. Hence, the local average magnetic field, $\langle \mathbf{B} \rangle$, is approximately equal to $\hat{\mathbf{x}} B_{xo}$. In other words, $\langle \mathbf{B} \rangle$ is highly aligned with the wave normal direction.

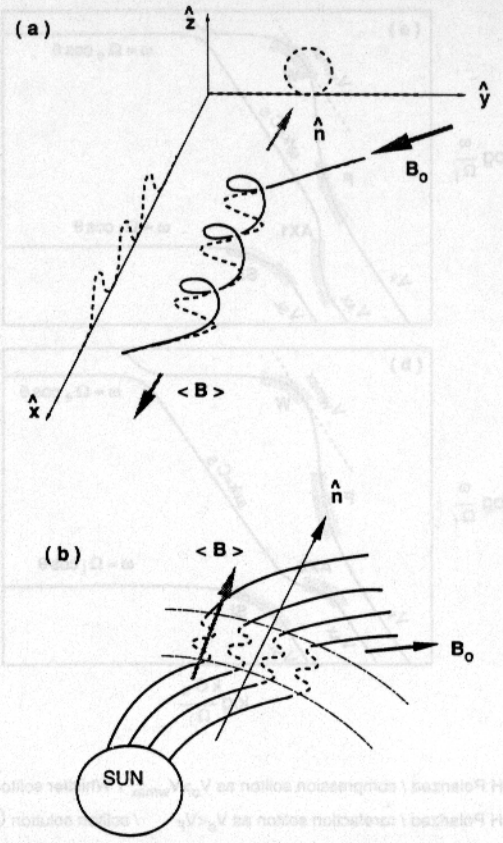

Fig. 10. (*a*) The three-dimensional magnetic field line structure of an obliquely propagating nonlinear Alfvénic wave. The solid curve is the magnetic field line, the dashed curves are the field line projections on the x-y, x-z, y-z planes. (*b*) The field line projection on the ecliptic plane for a nonlinear finite-extent Alfvén wave-train propagating outward from the sun. It can be seen that the upstream field $\mathbf{B}_o$ is different from the local average field $\langle \mathbf{B} \rangle$, while $\langle \mathbf{B} \rangle$ is highly aligned with the wave normal $\hat{\mathbf{n}}$.

The existence of finite-extent Afvén wave train solution has been discussed in section 3.2. The magnetic field line configuration of such a solution for oblique propagation can be sketched as illustrated in Figure 10*a* to show the relationship of $\hat{\mathbf{n}}$, $\mathbf{B}_o$ and $\langle \mathbf{B} \rangle$. Since the upstream magnetic field is given by $\mathbf{B}_o = \hat{\mathbf{x}} B_{xo} + \hat{\mathbf{y}} B_{yo}$ in our formulation, the local average field $\langle \mathbf{B} \rangle$ is shown to be different from $\mathbf{B}_o$. The assumption that $\mathbf{B}_o \simeq \langle \mathbf{B} \rangle$, as has been commonly adopted in the literature, is inconsistent with the solutions as shown in Figure 10*a*. The solid curve in Figure 10*a* is the field line and the dashed curves are the projection of the field line in the x-y, x-z, and y-z, planes. Figure 10*b* sketches the magnetic field line projection on the ecliptic plane for a finite-extent wave train propagating outward from the Sun, in which the wave energy flows along the magnetic field line but the wave normal direction is oblique to the upstream magnetic field. As can be seen from Figure 10*b*, the local average field $\langle \mathbf{B} \rangle$ is turned away from the upstream $\mathbf{B}_o$ direction to become aligned with $\hat{\mathbf{n}}$ when a nonlinear hydromagnetic wave is passing through.

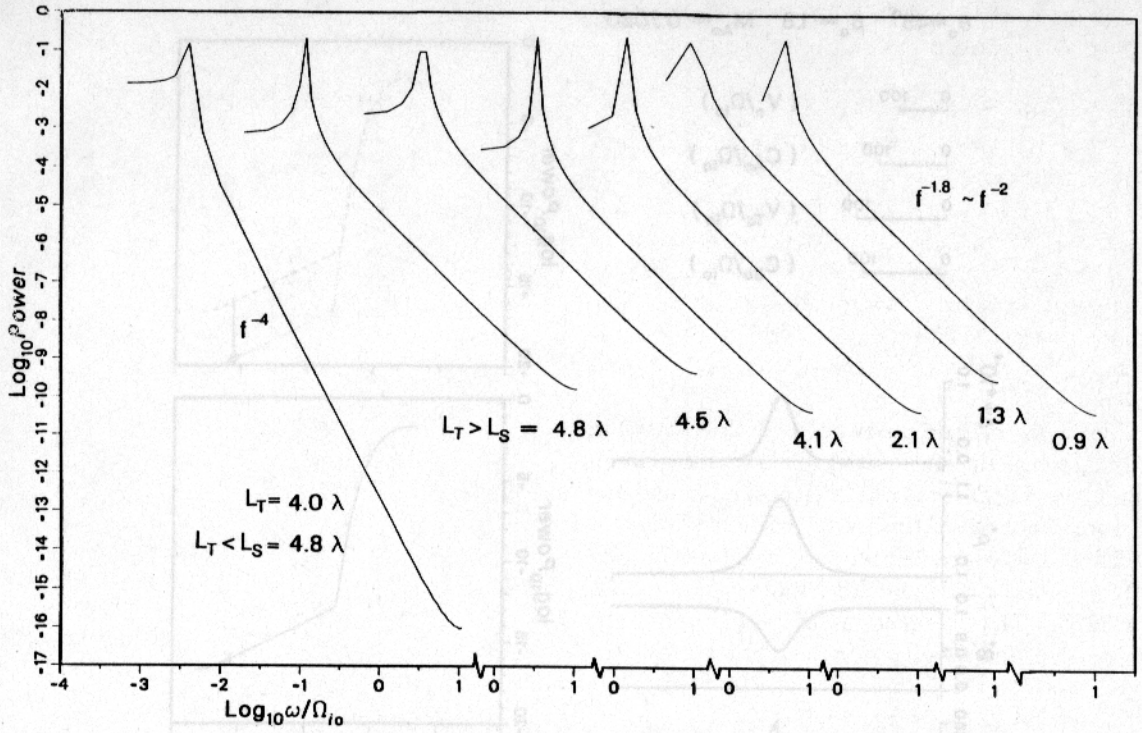

Fig. 11. Power spectra of wave magnetic field of finite-extent Alfvén wave train soluions. The first curve from the left is obtained for sampling length $L_S = 4.8\lambda$, while the length of the wave train is $L_T = 4\lambda$, where λ is the wavelength. The remaining curves are obtained for $L_T > L_S$ and L_S is not a integer of λ as indicated on each curve. The power spectrum shows a frequency dependence of $\sim f^{-4}$ when the sampling length cover the complete wave train, but shows a frequency dependence of $f^{-2} \sim f^{-1.8}$ when the sampling length contains incomplete wave periods. The latter result is consistent with observations [*Belcher and Davis*, 1971].

There are at least two possible causes for occasional deviations between $\langle \mathbf{B} \rangle$ and $\hat{\mathbf{n}}$ as observed. According to the results given in section 3, it can be shown that the angular deviation between the two vectors $\langle \mathbf{B} \rangle$ and $\hat{\mathbf{x}} B_{xo}$ increases as the difference between V_o and V_{AXo} increases. However, this explanation is only good for the short-wavelength Alfvénic fluctuations. For the long-wavelength wave train structures, the deviation may result from sampling over incomplete wave periods of a wave train structure. Sampling of incomplete wave periods can also provide a power spectrum with a frequency dependence of $f^{-1.8}$ to $f^{-2.0}$ as shown in Figure 11. The latter result is consistent with the observations ($f^{-1.5}$ to $f^{-2.2}$) given by *Belcher and Davis* [1971].

4.3. *Enhanced Power Spectrum at High Frequency Range*

The power spectrum of the observed Alfvénic fluctuations exhibits a hump in the high frequency range when the density fluctuation is present [e.g., *Unti et al.*, 1973; *Unti and Russell*, 1976; *Neugebauer et al.*, 1978]. The frequency of the hump is observed to be equivalent to a few tens of ion gyroradii [e.g., *Unti et al.*, 1973; *Neugebauer*, 1975, 1976; *Unti and Russell*, 1976; *Neugebauer et al.*, 1978].

The power spectrum of soliton solutions obtained in section 3 exhibits a plateau at frequency range which depends on the scale length of the soliton solution. The scale length of the soliton varies with upstream parameters β_o, θ_o, and M_{Ao}. The typical scale length is estimated to be about a few tens of the ion inertial length.

Figure 12 shows numerical integration results of soliton solution 6 as an example to illustrate the spatial scale length and the power spectrum of the two-fluid soliton solutions. The thickness of the soliton structure can be obtained based on the rulers shown on the upper-left corner. The unit of the first ruler, V_o/Ω_{io}, is the length scale used in the governing equations. The unit of the second ruler, C_{Ao}/Ω_{io}, is the ion inertial length (c/ω_{pi}). The unit of the last two rulers, V_{To}/Ω_{io} (with $V_{To} = \beta_o^{1/2} C_{Ao}$) and C_{So}/Ω_{io}, have been identified as the ion Larmor radius (R_L) respectively by *Lepping and Behannon* [1986] and *Stringer* [1963]. The maximum variation of $-\Delta\Psi$ in the first plot is less than 10^{-6} which indicates that the magnetic field hodogram of the solution follows closely the equipotential contour, which confirms the argument used in obtaining the analytic solutions discussed in section 3. Variations of $B^*(x)$ and $\rho^*(x)$ are out of phase as one of the characteristics of the analytic solution in 6. The rotation angle ϕ shows a variable rotation rate. Spatial pro-

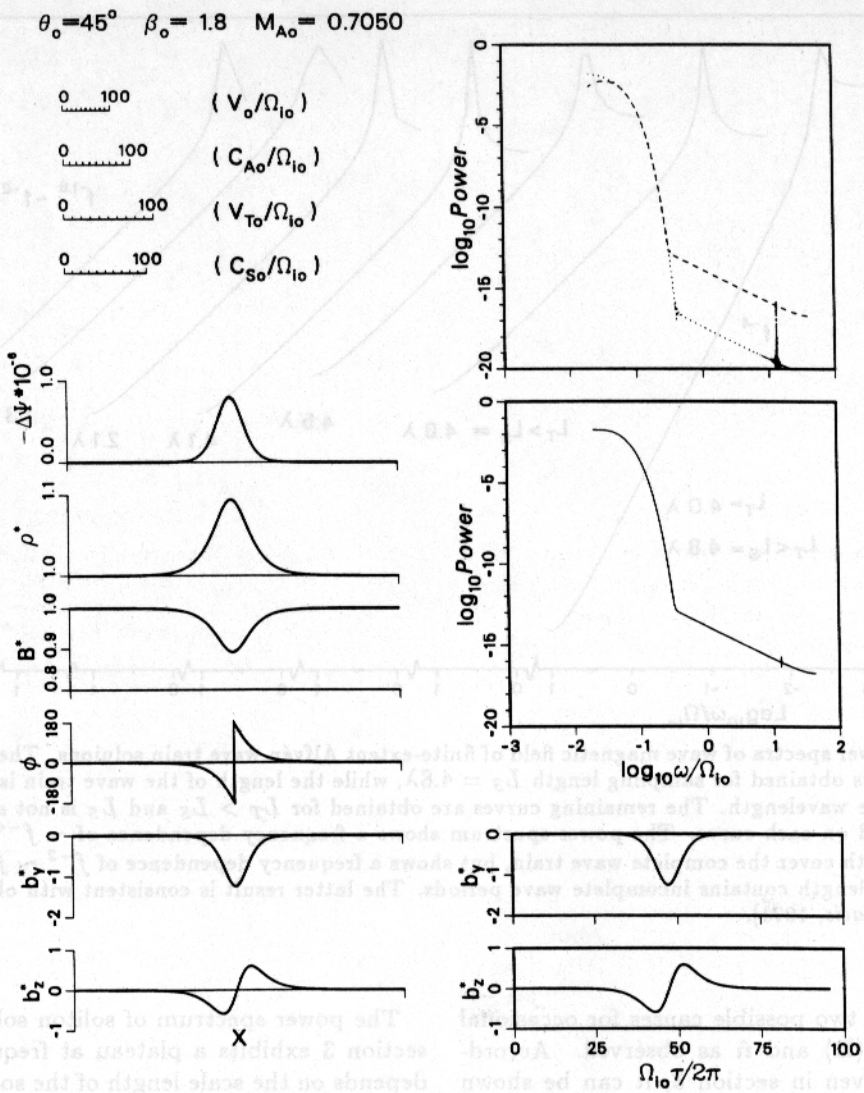

Fig. 12. Spatial profiles of a numerical soliton solution 6, and power spectra of the soliton magnetic field. The power spectra are plotted in arbitrary scale, in which the dotted, dashed, and solid curves are for $b_y(\omega)^2$, $b_z(\omega)^2$, and $b_y(\omega)^2 + b_z(\omega)^2$, respectively.

files of b_y^* and b_z^* are shown on the lower-left corner, whereas, $b_y^*(\tau)$ and $b_z^*(\tau)$ are shown on the lower-right corner, where $\tau = \int dx/V_x(x)$. The power spectra are obtained by sampling $b_y^*(\tau)$ and $b_z^*(\tau)$ curves in equal spacing. The power spectra are plotted in arbitrary scale, in which the dotted, dashed, and solid curves are for $b_y(\omega)^2$, $b_z(\omega)^2$, and $b_y(\omega)^2 + b_z(\omega)^2$, respectively. The plateau in the power spectrum is located at $\omega = 0.1\Omega_{io} \sim 0.01\Omega_{io}$ which is in reasonable agreement with observations [e.g., *Unti and Russell*, 1976]. A spiky structure appears near the lower hybrid frequency, indicating the presence of lower hybrid waves.

5. Discussion

Most of the early theoretical works [e.g., *Kakutani et al.*, 1967; *Crevier and Tidman*, 1970] claimed that $\dot{V}_x \to \infty$ when the local flow speed is equal to the sound speed, so that the quasi-neutrality assumption is inadequate as $M_S \to 1$. We have shown that $\dot{V}_x$ is finite when $M_S \to 1$. In addition, by considering the two-fluid linear dispersion relation, if the quasi-neutrality assumption is removed, the ion acoustic mode will have an additional dispersion near the ion Debye length [*Stringer*, 1963], which can lead to the formation of the ion acoustic soliton. However, it can be shown that the conversion of Alfvén mode to the ion acoustic wave can occur with or without the quasi-neutrality assumption. Hence the two-fluid rotational discontinuity solution obtained in this paper is a valid solution.

The parallel [*Spangler and Sheerin*, 1982; *Zharova and Litvak*, 1982; *Ovenden et al.*, 1983; *Spangler et al.*, 1985] and quasi-parallel [*Kennel et al.*, 1988] Alfvén envelop soliton solutions have been obtained from the deriva-

tive nonlinear Schrödinger (DNLS) equation. The parallel nonlinear Alfvén envelop solitons are shown to be unstable [*Machida et al.*, 1987] and nonlinearly damped [*Mjolhus and Wyller*, 1986]. The nonlinear damping is due to the combined effects of modulational instability and the resonant particle damping which is a kinetic effect in a finite-β plasma. The kinetic effect is absent in our model; parallel Alfvén soliton solutions are also absent in our model. We believe that the nonexistence of parallel Alfvén solitons in the two-fluid plasma indicates that these waves are either unstable or subject to disintegration regardless whether or not the kinetic effect is present in the model.

6. SUMMARY

We have presented a comprehensive set of nonlinear one-dimensional constant-profile isentropic wave solutions in finite-temperature two-fluid collisionless plasmas. These solutions not only can explain a variety of published observational results on Alfvénic fluctuations in the solar wind, but also predict certain features of nonlinear hydromagnetic waves for further observational study.

The oblique Alfvén wave train solutions, in the long wavelength limit, can explain the high degree of alignment between the local average magnetic field and the wave normal direction observed in the solar wind.

The two-fluid rotational discontinuity solution obtained in this study is highly circularly polarized, with scale length a few tens ion inertial length. The upstream flow speed of the rotational discontinuity must deviate slightly from the Alfvén-mode speed. This solution predicts that the downstream flow speed of the two-fulid rotational discontinuity must be equal to the local sound speed. This result is due to the wave dispersion which converts the Alfvén mode to the ion acoustic mode to form the two-fluid rotational discontinuity. The variable rotation rate, the 180° rotation limit, and the thickness of the two-fluid rotational discontinuity provide a satisfactory theoretical explanation for the rotational discontinuity structures observed in the solar wind.

For upstream flow speed less than the fast-mode speed, soliton solutions include rarefaction fast solitons, compression slow solitons, and Alfvén solitons. The Alfvén solitons are super-Alfvénic compression waves if the upstream Alfvén-mode speed is greater than the sound speed; otherwise, they are sub-Alfvénic rarefaction waves. The scale length of these soliton solutions are all of a few tens of ion inertial length. The power spectrum of the soliton solutions can explain the observed power spectrum which exhibits an enhanced hump in high frequency range.

The density and magnetic field variations of nonlinear hydromagnetic waves with upstream flow speed less than the fast mode speed are shown to obey the following two rules. (1) All compression waves are left-hand polarized and all rarefaction waves are right-hand polarized, due to the ion inertial effect. (2) The density variation and the magnetic field magnitude variation are in phase if the flow is supersonic, but out of phase if the flow is subsonic. The result in (2) is a consequence of the conservation of momentum flux.

Acknowledgments. This work was supported inpart by NSF grant under Atmospheric Science Section: ATM 85-21194 to the University of Alaska Fairbanks.

The Editor thanks S. R. Spangler and another referee for their assistance in evaluating this paper.

REFERENCES

Barnes, A., Interplanetary Alfvénic fluctuations: A stochastic model, *J. Geophys. Res., 86*, 7498, 1981.

Barnes, A., Hydromagnetic turbulence in the interplanetary medium, in *Solar Terrestrial Physics, Principles and Theoretical Foundations*, edited by R. L. Carovillano and J. M. Forbes, p. 172, D. Reidel, Hingham, Mass., 1983.

Belcher, J. W., and L. Davis, Jr., Large-amplitude Alfvénic waves in the interplanetary medium, *J. Geophys. Res., 76*, 3534, 1971.

Berchem, J. W., and C. T. Russell, The thickness of the magnetopause current layer: ISEE 1 and 2 observations, *J. Geophys. Res., 87*, 2108, 1982*a*.

Berchem, J. W., and C. T. Russell, Magnetic field rotation through the magnetopause: ISEE 1 and 2 observations, *J. Geophys. Res., 87*, 8139, 1982*b*.

Burlaga, L. F., J. F. Lemaire, and J. M. Turner, Interplanetary current sheets at 1 AU, *J. Geophys. Res., 82*, 3191, 1977.

Cavaliere, A., and F. Engelmann, Laminar hydromagnetic waves of finite amplitude in plasmas of low temperature, *Nucl. Fusion, 7*, 137, 1967.

Churilov, S. M., Steady MHD flows of a finite-β plasma, *Sov. J. Plasma Phys., 6*, 377, 1980.

Coroniti, F. V., Laminar wave-train structure of collisionless magnetic slow shocks, *Nucl. Fusion, 11*, 261, 1971.

Crevier, W. F., and D. A. Tidman, Oblique shocks in finite-beta plasmas, *Phys. Fluids, 13*, 2275, 1970.

Daily, W. D., Alfvén wave refraction by interplanetary inhomogeneities, *J. Geophys. Res., 78*, 2043, 1973.

Davis, L., R. Lüst, and A. Schlüter, The structure of hydromagnetic shock waves, I, Nonlinear hydromagnetic waves in a cold plasma, *Z. Naturforsch., 13a*, 916, 1958.

Denskat, K. U., and F. M. Neubauer, Statistical properties of low-frequency magnetic field fluctuations in the solar wind from 0.29 to 1.0 AU during solar minimum conditions: Helios 1 and Helios 2, *J. Geophys. Res., 87*, 2215, 1982.

Fishman, F. J., A. R. Kantrowitz, and H. E. Petschek, Magnetohydrodynamic shock wave in a collision-free plasma, *Rev. Mod. Phys., 32*, 959, 1960.

Formisano, V., and C. F. Kennel, Small amplitude waves in high β plasmas, *J. Plasma Phys., 3*, 55, 1969.

Goodrich, C. C., and J. D. Scudder, The adiabatic energy change of plasma electrons and the frame dependence of the cross-shock potential at collisionless magnetosonic shock waves, *J. Geophys. Res., 89*, 6654, 1984.

Hain, K., R. Lüst, and A. Schlüter, Hydromagnetic waves of finite amplitude in a plasma with isotropic and non-isotropic pressure perpendicular to a magnetic field, *Rev. Mod. Phys., 32*, 967, 1960.

Hollweg, J. V., Alfvén wave refraction in high-speed solar wind streams, *J. Geophys. Res., 80,* 908, 1975.

Hudson, P. D., Rotational discontinuities in an anisotropic plasma, *Planet. Space Sci., 19,* 1693, 1971.

Hudson, P. D., Rotational discontinuities in an anisotropic plasma, II, *Planet. Space Sci., 21,* 475, 1973.

Kakutani, T., T. Kawahara, and T. Taniuti, Nonlinear hydromagnetic solitary waves in a collision-free plasma with isothermal electron pressure, *J. Phys. Soc. Jpn., 23,* 1138, 1967.

Kantrowitz, A., and H. E. Petschek, MHD characteristics and shock waves, in *Plasma Physics in Theory and Application*, edited by W. B. Kunkel, p. 148, McGraw-Hill, New York, 1966.

Kellogg, P. J., Solitary waves in cold collisionless plasma, *Phys. Fluids, 7,* 1555, 1964.

Kennel, C. F., B. Buti, T. Hada, and R. Pellat, Nonlinear, dispersive, elliptically polarized Alfvén waves, *Phys. Fluids, 31,* 1949, 1988.

Lepping, R. P., and K. W. Behannon, Magnetic field directional discontinuities: Characteristics between 0.46 and 1.0 AU, *J. Geophys. Res., 91,* 8725, 1986.

Machida. S., S. R. Spangler, and C. K. Goertz, Simulation of amplitude-modulated circularly polarized Alfvén waves for beta less than one, *J. Geophys. Res., 92,* 7413, 1987.

Martin, R. N., J. W. Belcher, and A. J. Lazarus, Observations and analysis of abrupt changes in the interplanetary plasma velocity and magnetic field, *J. Geophys. Res., 78,* 3653, 1973.

Matthaeus, W. H., and M. L. Goldstein, Measurement of the rugged invariants of magnetohydrodynamic turbulence in the solar wind, *J. Geophys. Res., 87,* 6011, 1982.

Mjolhus, E., and J. Wyller, Alfvén solitons, *Phys. Scripta, 33,* 442, 1986.

Montgomery, D., Nonlinear Alfvén waves in a cold ionized gas, *Phys. Fluids, 2,* 585, 1959.

Morton, K. W., Finite amplitude compression waves in a collision-free plasma, *Phys. Fluids, 7,* 1800, 1964.

Neugebauer, M., The enhancement of solar wind fluctuations at the proton thermal gyroradius, *J. Geophys. Res., 80,* 998, 1975.

Neugebauer, M., Corrections to and comments on the paper "The enhancement of solar wind fluctuations at the proton thermal gyroradius," *J. Geophys. Res., 81,* 2447, 1976.

Neugebauer, M., C. S. Wu, and J. D. Huba, Plasma fluctuations in the solar wind, *J. Geophys. Res., 83,* 1027, 1978.

Ovenden, C. R., H. A. Shah, and S. J. Schwartz, Alfvén solitons in the solar wind, *J. Geophys. Res., 88,* 6095, 1983.

Petschek, H. E., Aerodynamic dissipation, *Rev. Mod. Phys., 30,* 966, 1958.

Saffman, P. G., On hydromagnetic waves of finite amplitude in a cold plasma, *J. Fluid Mech., 11,* 552, 1961.

Sagdeev, R. Z., Cooperative phenomena and shock waves in collisionless plasmas, *Rev. Plasma Phys., 4,* 23, 1966.

Solodyna, C. V., and J. W. Belcher, On the minimum variance direction of magnetic field fluctuations in the azimuthal velocity structure of the solar wind, *Geophys. Res. Lett., 3,* 565, 1976.

Sonnerup, B. U. Ö., and L. J. Cahill, Jr., Magnetopause structure and attitude from Explorer 12 observations, *J. Geophys. Res., 72,* 171, 1967.

Sonnerup, B. U. Ö., and L. J. Cahill, Jr., Explorer 12 observations of the magnetopause current layer, *J. Geophys. Res., 73,* 1757, 1968.

Sonnerup, B. U. Ö., and B. G. Ledley, Magnetopause rotational forms, *J. Geophys. Res., 79,* 4309, 1974.

Spangler, S. R., and J. P. Sheerin, Properties of Alfvén solitons in a finite-beta plasma, *J. Plasma Phys., 27,* 193, 1982.

Spangler, S. R., J. P. Sheerin, and G. L. Payne, A numerical study of nonlinear Alfvén waves and solitons, *Phys. Fluids, 28,* 104, 1985.

Stringer, T. E., Low-frequency waves in an unbounded plasma, *Plasma Phys. J. Nucl. Energy, Part C, 5,* 89, 1963.

Swift, D. W., and L. C. Lee, Rotational discontinuities and the structure of the magnetopause, *J. Geophys. Res., 88,* 111, 1983.

Unti, T., and C. T. Russell, On the causes of spectral enhancements in solar wind power spectra, *J. Geophys. Res., 81,* 469, 1976.

Unti, T. W. J., M. Neugebauer, and B. E. Goldstein, Direct measurements of solar-wind fluctuations, *Astrophys. J., 180,* 591, 1973.

Zharova, N. A., and A. G. Litvak, Nonlinear envelope Alfvén waves in a magnetized plasma, *Sov. J. Plasma Phys., 8,* 552, 1982.

Ziegler, H. J., and K. Schindler, Structure of subcritical perpendicular shock waves, *Phys. Fluids, 31,* 570, 1988.

J. R. Kan and L. H. Lyu, Geophysical Institute, University of Alaska, Fairbanks, C. T. Elvey Building, Fairbanks, AK 99775.

(Received January 12, 1988;
revised December 22, 1988;
accepted January 3, 1989.)